Published in final edited form as:
J Magn Reson Imaging. 2008 April ; 27(4): 809–817.

Simultaneous Imaging of Myocardial Motion and Chamber Blood Flow With SPAMM n' EGGS (Spatial Modulation of Magnetization With Encoded Gradients for Gauging Speed)

Smita Sampath, PhD[1], **June H. Kim, MD**[2], **Robert J. Lederman, MD**[1], and **Elliot R. McVeigh, PhD**[1,*]

[1]*Laboratory of Cardiac Energetics, National Heart, Lung, and Blood Institute, National Institutes of Health, DHHS, Bethesda, Maryland.* [2]*Cardiovascular Branch, Division of Intramural Research, National Heart, Lung, and Blood Institute, National Institutes of Health, DHHS, Bethesda, Maryland.*

Abstract

Purpose: To provide simultaneous measurements of one-dimensional (1-D) myocardial displacement and 1-D chamber blood flow in a single breath-held acquisition using an MR imaging technique, SPAMM n' EGGS (Spatial Modulation of Magnetization With Encoded Gradients for Gauging Speed).

Materials and Methods: Velocity encoding bipolar gradients sensitive to chamber blood flow were played out before the readout gradient in a 1-1 SPAMM-tagged MR imaging pulse sequence. For any given motion–flow encoded direction, the acquired image sequence was later postprocessed to separate the tag motion and blood flow terms. Experiments were performed on seven normal volunteers, and two pigs with moderate ischemic mitral regurgitation. Left-ventricular motion and trans-valvular flow obtained using the SPAMM n' EGGS pulse sequence was compared against measurements obtained using standard tagging and phase-contrast pulse sequences, respectively.

Results: Results in normal volunteers and diseased pigs demonstrate multiphase correlated measurements of myocardial motion and chamber blood flow using SPAMM n' EGGS. A close correspondence in these measurements to conventional tagging and phase-contrast sequences is confirmed.

Conclusion: We have demonstrated that simultaneous acquisition of myocardial motion and chamber blood flow is possible within a single breath-hold. The data obtained using the SPAMM n' EGGS pulse sequence may be useful in the planning and evaluation of mitral-valve repair procedures.

Keywords

myocardial motion; blood flow; velocity; tagging; phase-contrast; SPAMM; MRI

Correlated Measurements of myocardial motion and chamber blood flow may provide useful diagnostic information and procedural feedback in patients with ischemic mitral regurgitation (IMR) (1), left ventricular (LV) hypertrophy (2), LV dilatative cardiomyopathy (3), and LV dyssynchrony (4), at rest and under stress. Although ultrasound-based imaging methods are the current state of the art, MR imaging has become well established as an important modality for imaging myocardial strain and trans-valvular blood flow.

*Address reprint requests to: S. Sampath, National Institutes of Health, National Heart Lung Blood Institute, Laboratory of Cardiac Energetics, Bldg 10, Room B1D-416 MSC 1061, Bethesda, MD 20892-1061. E-mail: sampaths@mail.nih.gov

Methods such as MR tagging (5,6), phase contrast (7-10), or stimulated echo imaging (11-13) provide precise measurements of regional and global wall motion, while phase contrast methods have also demonstrated the capability to measure intracardiac flows (14-16), and compute regurgitant flow volumes (17,18). In this study, we present a new MR imaging method, called SPAMM n' EGGS (spatial modulation of magnetization acquisitions with encoded gradients for gauging speed), that combines tagging and phase-contrast imaging principles to provide simultaneous, correlated, spatially and temporally registered measurements of one-dimensional (1-D) tissue motion and 1-D chamber blood flow in any desired slice orientation in the heart in a single breath-held acquisition using a unified imaging protocol. This is achieved by playing a velocity encoded bipolar gradient sensitive to chamber blood flow before the readout gradient in a 1-1 SPAMM-tagged MR imaging pulse sequence. The sequence of images obtained is later postprocessed to separate the motion and flow terms. On a four-chamber slice, for example, the data acquired permits the simultaneous time-resolved examination of the left-ventricular myocardial strain patterns and blood flow patterns across the mitral valve and the aortic valve. This technique may provide valuable feedback on the interplay between tissue dynamics and chamber blood flow before, during, and after surgical procedures (e.g., mitral valve repair) in multiple representative slice orientations. Any physiologic transient events (for example, stress) that occur during the acquisition will be manifested in a correlated manner on both the motion and the flow data sets as they are acquired simultaneously.

Visualization tools provide the simultaneous display of this motion and flow data in a semiautomated manner offline. Results obtained in normal volunteers (n = 7) and two pigs with moderate induced IMR are presented in this study. The synchronicity of the computed longitudinal shortening curves in the septum and the free wall and the flow curves across the mitral valve and the aortic valve is examined. A comparison of these measurements against those obtained using conventional tagging and phase-contrast pulse sequences is also presented. In the following section, we first describe the 1-1 SPAMM tagging equation and later extend it to derive the image equations for SPAMM n' EGGS.

THEORY

A typical SPAMM n' EGGS pulse sequence comprises a gradient echo readout with (i) a 1-1 SPAMM (19) tagging preparation, and (ii) a bipolar gradient pulse played out just before the readout gradient. The resultant longitudinal magnetization signal is similar to a standard 1-1 SPAMM tagging signal with the exception that a velocity-encoded phase term is now added to the signal. This can be mathematically represented as follows:

$$I(\mathbf{p},t) = \{f_1(\mathbf{p},t,T_1(\mathbf{p}))\, M_0(\mathbf{p}) \cos(\varphi_x(\mathbf{p},t)) + f_2(\mathbf{p},t,T_1(\mathbf{p}))\, M_0(\mathbf{p})\}\, e^{j\theta(\mathbf{p})} e^{j\varphi_{vx}(\mathbf{p},t)}. \quad [1]$$

where, $\mathbf{p} \equiv (x,y)$ is the position vector of a point in the 2-D image, t is the image time stamp, $M_0(\mathbf{p})$ is the longitudinal steady state magnetization signal averaged over the imaged slice, and f_1 and f_2 are conversely related rate functions that control the tag signal decay and the recovery of the steady-state longitudinal magnetization respectively. In Eq. [1], it is assumed that the tags are applied along the phase-encode direction (say y-axis), while the bipolar gradient is applied along the readout direction (say x-axis). The tagging sinusoidal modulation function is represented by the term $\cos(\phi_x(\mathbf{p},t))$, while the velocity encoded phase term is represented by $\phi_{vx}(\mathbf{p},t)$. The additive phase term $\theta(\mathbf{p})$ accounts for any phase accumulation as a result of inhomogeneities in the magnetic field. For this application, differential off-resonant phase error contributions in the three peaks due to the tagging and readout gradients have negligible effects and are ignored in Eq. [1].

Now, if we take the magnitude of the image sequence described in Eq. [1], we get a sequence of standard 1-1 SPAMM-tagged magnitude images (see panel B in Fig. 1).

$$|I(\mathbf{p},t)| = |f_1(\mathbf{p},t,T_1(\mathbf{p}))\, M_0(\mathbf{p}) \cos \quad (\varphi_x(\mathbf{p},t)) + f_2(\mathbf{p},t,T_1(\mathbf{p}))\, M_0(\mathbf{p})|. \quad [2]$$

Cardiac motion and strain can be computed from these tagged images using previously published postprocessing techniques (20,21). The tag contrast in the myocardium is mainly dependent on the exponentially decaying function $f_1(\mathbf{p},t; T_1^{\text{myocardium}}(\mathbf{p}))$ and the rate of tag decay in the myocardium can be controlled by designing an appropriate sequence of imaging flip angles. This is examined in detail in the methods section below.

Previous studies (15) have indicated the presence of sinuous, and chirally asymmetric flow patterns within the chambers of the heart during systole. This rapid asymmetric in-plane and through-plane mixing causes tag shearing, and destructive interference of tagging modulations within the blood pool resulting in a rapid decay of tags within the chambers of the heart. Using a standard 1-1 SPAMM tagging pulse sequence with a total tagging flip angle of 180°, we found that the time of decay within all chambers of the heart was within 100 ms. Thus, Eq. [2]. can be approximated by

$$I_{blood}(\mathbf{p},t) = \left\{ f_2\left(\mathbf{p},t,T_1^{blood}(\mathbf{p})\right) M_0(\mathbf{p}) \right\} e^{j\theta(\mathbf{p})} e^{j\varphi_{vx}(\mathbf{p},t)} \quad [3]$$

for those pixels **p** that lie within the blood pool, and the phase of these image pixels can be expressed as:

$$\varphi_{blood}(\mathbf{p},t) = \theta(\mathbf{p}) + \varphi_{vx}(\mathbf{p},t). \quad [4]$$

To separate the velocity encoded flow term from the field inhomogeneity phase term in Eq. [4], the velocity encoding gradients are turned off every odd cardiac frame. These velocity unencoded reference images with blood phase $\varphi_{blood}^{ref}(\mathbf{p},t) = \theta(\mathbf{p})$ are then used to perform a sliding-window phase-sensitive reconstruction operation (see Fig. 1A):

$$\frac{I(\mathbf{p},t)\, I_{ref}(\mathbf{p},t)^*}{|I(\mathbf{p},t)|\,|I_{ref}(\mathbf{p},t)|}, \quad [5]$$

Taking the phase of the resultant image within the blood pool we then get

$$\varphi_{blood}(\mathbf{p},t)\, \varphi_{blood}^{ref}(\mathbf{p},t)^* = \varphi_{vx}(\mathbf{p},t). \quad [6]$$

Thus, the velocity-encoded flow terms are isolated (see panel A in Fig. 1). The strength of the chamber blood flow signal is dominated by the exponentially increasing function $f_2(\mathbf{p},t; T_1^{\text{blood}}(\mathbf{p}))$ and its rate of recovery can be controlled by designing an appropriate sequence of imaging flip angles (see methods section below for more details).

METHODS

Imaging Pulse Sequence

All experiments were conducted on a 1.5 Tesla (T) Siemens Espree scanner (Siemens Medical Solutions, Erlangen, Germany) equipped with gradient coils capable of imaging at 33 mT/m and with maximum slew rates of 100 T/m/s. The SPAMM n' EGGS pulse sequence timing diagram, with displacement and velocity sensitivities along the phase encode direction, is shown in Figure 2. The sequence mainly comprises a 1-1 SPAMM tagging preparation module triggered by the R-wave followed by a gated, sequential, multiphase 2D gradient-echo imaging sequence. Two nonselective radio frequency (RF) rectangular pulses of equal area separated by a tagging gradient were designed to create 1-1 SPAMM tags in the image. Crusher gradients

were applied along the readout and phase-encode axes after the tag preparation to spoil any residual transverse magnetization. To achieve sensitivity to chamber blood velocity, bipolar gradient pulses were played out every even cardiac phase along the readout axis before the readout gradient (see rectangular boxes in Fig. 2). The first moment of the gradients on the readout and the slice axes were nulled at the center of the echo to provide flow compensation along these axes. The timings of the readout prephase gradients for the unencoded and the flow-encoded cardiac phases were made equal, to ensure the background phase is cancelled out when performing the phase-sensitive reconstruction (see Eq. [10]) of the flow signal. The phase encode gradients were rewound and a z-crusher gradient was played out at the end of each readout acquisition. Typical imaging parameters used were as follows: imaging matrix 192 × 160, receiver bandwidth ±48 KHz, resolution 1.6 mm × 1.6 mm, slice thickness 8-10 mm, echo time (TE) 4 ms, repetition time (TR) 8 ms, views per cardiac phase 3–5, tag separation 8 mm, and V_{enc} 90 cm/s. With these imaging parameters, a temporal resolution of around 40 ms was achieved, resulting in a scan duration of 30 s.

To maintain an optimal compromise between tag persistence in diastole and early recovery of the flow signal in systole, the incrementing train of imaging flip angles prescribed in previous literature (22) was modified and implemented. This new sequence of imaging flip angles, α_i, was designed as

$$\alpha_i = \alpha \tan\left(\sin(\alpha_{i+1})\, e^{-TR/T_1}\right) + (\gamma \times (n-1)) / (n-1), \quad [7]$$

where the second additive term in Eq. [11]. is a ramp-down function in time. The number of imaging RF pulses is denoted by n, and γ is the slope factor for the ramp-down function.

The family of curves for the functions $f_1(\mathbf{p},t;\alpha,n,T_1^{\text{myocardium}}(\mathbf{p}))$, and $f_2(\mathbf{p},t;\alpha,n,T_1^{\text{blood}}(\mathbf{p}))$ were simulated for a range of (i) imaging final flip angles α_n, and (ii) slope factor γ to identify optimal parameter values that maximize the area under the curves for both functions over the entire cardiac cycle. From these simulations, an α_n of 10–15°, and a γ of 5° provided a good compromise between tag signal fading and flow signal relaxation for a typical acquisition comprising 85 RF pulses.

Experiments

First, to evaluate the performance of the SPAMM n' EGGS sequence, we compared two quantities—the tag contrast and the noise estimate in the flow signal—for a range of tagging flip angles (β = 45°–90°) against corresponding measurements obtained using conventional tagging and conventional phase contrast sequences respectively in a normal volunteer. All normal volunteer experiments were approved by the Institutional Review Board of the National Heart Lung and Blood Institute and informed consent was obtained from all volunteers. The conventional tagging sequence comprised a 1-2-3-2-1 SPAMM with a tagging flip angle of 65° followed by a gated, segmented, gradient-echo-based image acquisition. The conventional phase-contrast sequence was a gated, segmented, gradient-echo–based image sequence with alternating velocity encoding bipolar gradient polarities every alternate cardiac phase. Imaging parameters described in the previous section were used for the SPAMM n' EGGS acquisition, and identical spatial resolutions, field of view, and motion/flow encoding imaging parameters were used in the conventional scans. For a four-chamber slice acquired, the tag signal in a mid-ventricular region of interest (ROI) in the septal wall was averaged along the direction of the tags. The difference between the peak and trough of the resultant sinusoidal tag signal for that ROI was then defined as the tag contrast. To characterize the noise in the flow signal, a rectangular region of interest was defined near the aortic outflow and the mitral inflow. To eliminate any flow variations within that region of interest, a high-pass Kaiser filter was first used in *k*-space. The noise estimate (in centimeters per second) was then defined as the root

mean square of the differences in the velocity measurements between all adjacent pairs of pixels in the region of interest.

Next, to evaluate the accuracy of the technique, we compared myocardial strain and trans-valvular flow measurements obtained using SPAMM n' EGGS (with a fixed tagging flip angle of 65°) with those obtained using conventional tagging and phase-contrast scans in six normal volunteers. The lateral or septal longitudinal strains were obtained by fitting pure sinusoidal curves to tagging patterns across representative regions selected at each time frame and computing the percentage rate of change in the frequency of these sinusoidal curves with respect to the first time frame. The trans-valvular flows were computed by selecting rectangular trans-mitral and trans-aortic regions of interest and computing the average velocity of all pixels within these regions.

Finally, animal experiments were conducted to evaluate the feasibility of this technique in detecting motion and flow dysfunctions in pigs with an induced model of ischemic mitral regurgitation. All animal experiments were approved by the National Heart Lung and Blood Institute Animal Care and Use Committee, and conducted under inhalation anesthesia and mechanical ventilation. Mild–moderate ischemic mitral valve regurgitation was created by serial transcoronary ethanol ablation of the posterior-lateral wall of the left ventricle. During each ablation procedure, 2 weeks apart, 1–3 mL of pure ethanol was administered into different marginal branches of the circumflex coronary artery through the guidewire port of a balloon angioplasty catheter. Imaging was conducted at least 4 weeks after the first myocardial infarction procedure, and demonstrated mitral valve regurgitation on balanced steady-state precession (b-SSFP) MRI. For both pigs, SPAMM n' EGGS data was acquired in a four-chamber slice for two orthogonal motion–flow directions in two short breath-held acquisitions. For these experiments, a temporal resolution of 20 ms with breath-hold times of approximately 40 s was achieved.

Data Visualization

Postprocessing software was developed in MATLAB 7.0 (The Mathworks Inc, Natick, MA) to provide a visual display of the tagged myocardium overlaid on color-coded blood velocity data. Two user-contoured masked regions, one isolating the tagged myocardium from the sequence of images obtained using Eq. [2], and the other isolating the flow in the inner chambers of the heart from the images obtained using Eq. [6], were combined into a single SPAMM n' EGGS image display $C(\mathbf{p},t)$. The images were converted to RGB images with the tagged myocardium scaled using a bone (grayscale with a bluish tinge) colormap and the flow images scaled using an hsv colormap. To visualize 2-D myocardial motion and 2-D blood flow information, data obtained from two orthogonally encoded SPAMM n' EGGS acquisitions from two separate breath-holds were combined. Bi-directional flow was visualized by generating 2-D velocity vector plots overlaid on the image sequence $C(\mathbf{p},t)$.

RESULTS

Studies were conducted in seven normal volunteers and two pigs with induced ischemic mitral regurgitation. The results obtained from these studies are depicted in Figures 3-8 and Table 1.

Figure 3a-d qualitatively compares the reconstructed tagged images obtained using SPAMM n' EGGS for three different tagging flip angles of 45° (see Fig. 3a), 65° (see Fig. 3b), 90° (see Fig. 3c) at three representative time frames, and using the conventional tagging sequence (see Fig. 3d) at correspondingly close time frames. Figure 3e-h qualitatively compares the reconstructed flow images obtained using SPAMM n' EGGS for three different tagging flip angles of 45° (see Fig. 3e), 65° (see Fig. 3f), 90° (see Fig. 3g) at three representative time frames, and the conventional phase contrast sequence (see Fig. 3h) at correspondingly close

time frames. As would be expected, it is clear that as the tagging flip angle increases, the tag contrast in the SPAMM n' EGGS-tagged images improves later in the cardiac cycle. From the SPAMM n' EGGS flow images, it is clearly evident that as the tagging flip angle increases, the flow signal early in the cardiac cycle is suppressed due to saturation of the blood signal.

Plots of the evolution of tag contrast and the noise estimate in the flow signals are seen in Figure 4. Figure 4a compares the tag contrast from SPAMM n' EGGS acquisitions (solid lines) with tagging flip angles in the range of (90°–170°) with increments of 20° and a conventional tagging (dot-dashed line) acquisition. Figure 4b compares the noise estimate in the flow signal from SPAMM n' EGGS acquisitions (solid lines) with tagging flip angles in the range of (90°–170°) with increments of 20° and a conventional flow (dot-dashed line) acquisition. From Figure 4a, we find that the overall tag contrast improves with larger tagging flip angles. We also find that the conventional tagging sequence demonstrates better tag contrast through most of the cardiac cycle. From Figure 4b, we find that the noise estimates in the SPAMM n' EGGS flow measurements early in the cardiac cycle are higher for larger tagging flip angles and these estimates asymptotically approach the noise estimates for the conventional flow sequence.

Differences in longitudinal strain and blood velocity measurements obtained using SPAMM n' EGGS with a tagging flip angle of 65° and conventional tagging and phase contrast sequences for a normal volunteer are depicted in Figure 5. Figure 5a displays time evolution curves for aortic flow and mitral flow averaged in two rectangular regions of interest. The curves demonstrate similar trends in both cases. Figure 5b displays time evolution curves for lateral and septal longitudinal strains. Again, the curves demonstrate similar trends in both cases. Table 1 compares eight key parameters of interest obtained from such curves in six healthy volunteers. These are peak septal longitudinal shortening, time to peak septal longitudinal shortening, peak lateral longitudinal shortening, time to peak lateral longitudinal shortening, peak arotic outflow, time to peak aortic outflow, peak mitral inflow, and time to peak mitral inflow. These results again demonstrate close correspondence in measurements.

Figure 6 displays the combined tagged images with color flow overlay for eight representative time frames of a four-chamber slice obtained in a normal volunteer. The hsv colormap used to scale the blood-flow is also displayed. The first row depicts images acquired during the systolic phase, while the second row depicts images acquired during the diastolic phase. Longitudinal shortening during systole and longitudinal relaxation during diastole is clearly visualized from the tagged data. The tagged data persist through 700 ms of the acquisition. The aortic outflow (in blue and purple) during systole and the mitral inflow (green, yellow and orange) during diastole is also clearly visualized from these images. The flow signal strength within the blood pool recovers to an acceptable degree within 100 ms of the cardiac cycle. From these images, it is evident that significant systolic outflow initiates before considerable longitudinal shortening has occurred, while peak diastolic inflow follows a few 100 ms after longitudinal relaxation in the ventricle has initiated.

Combined motion–flow images obtained from one of the pig studies is displayed in Figure 7 for six key time frames. From these images, a regurgitant jet is clearly visualized in the first three time frames. To appreciate the directional information of the blood flow, data obtained from two SPAMM n' EGGS acquisitions with orthogonally oriented flow sensitivities are combined and 2-D velocity vector plots are overlaid on the images. The jet velocity seems mostly coherent during the first two time frames and strongly oriented in the vertical direction, becoming more diffuse in the third time frame.

Figure 8a shows time evolution curves of aortic outflow velocity (marked 1), and mitral inflow velocity (marked 2) obtained from this normal volunteer by averaging the blood flow velocities computed from rectangular regions of interest depicted in Figure 6 (subimage 8). [Color Fig.

8 can be viewed in the online issue, which is available at www.interscience.wiley.com.] Time evolution curves of septal (marked 3) and lateral (marked 4) longitudinal strains in the same volunteer are also displayed. The blood velocity axis is marked on the left, while the myocardial longitudinal strain axis is marked on the right. Peak aortic outflow velocity of 45 cm/s, peak diastolic inflow velocity of −60 cm/s, and peak longitudinal shortening of −15% was observed in this volunteer. Note significant aortic outflow occurs when the heart has contracted longitudinally by approximately 17%, and lasts for approximately 100 ms, during which the heart contracts the fastest (from 17% to 80%). The peak diastolic inflow occurs when the lateral wall of the heart has longitudinally relaxed by 33%, and the septum has longitudinally relaxed by 75%. Here, we also observe that peak aortic outflow and peak diastolic inflow occur approximately 150 ms after the initiation of longitudinal shortening and longitudinal relaxation, respectively.

Figure 8b displays time evolution curves of aortic outflow velocity (marked 1), mitral regurgitant velocity (marked 2) and mitral inflow velocity (marked 3) obtained from the first IMR pig by averaging the blood flow velocities computed from rectangular regions of interest depicted in Figure 7 (subimage 4). Time evolution curves of lateral (marked 4) and septal (marked 5) longitudinal strains in the same volunteer are also displayed. Peak aortic outflow velocity of 25 cm/s, peak diastolic inflow velocity of −63 cm/s, peak mitral regurgitant outflow of 10 cm/s, peak septal longitudinal shortening of −14%, and peak lateral longitudinal shortening of −6% was observed in this pig. Here, we note that the peak aortic outflow velocity occurs before any notable longitudinal shortening initiates. From this point on, there is a gradual almost linear decrease in outflow velocity at a rate of 125 cm/s^2 over 200 ms until maximum septal longitudinal strain of 14% is achieved. Peak mitral regurgitation is observed around 125 ms into the cardiac cycle, when the heart has contracted by approximately 25%. Peak diastolic inflow occurs around 380 ms into the cardiac cycle when the septum has relaxed by approximately 70%. The diastolic vortices are formed after nearly 92% of ventricular relaxation has occurred. The lateral strain in the infarcted wall is much lower than the septal wall, as would be expected.

DISCUSSION

Treatment options for IMR are likely to evolve as catheter-based as other surgical procedures are introduced. The development, planning, and evaluation of mitral valve repair procedures could benefit from an imaging technique that provides rapid visual feedback on myocardial motion and chamber blood flow patterns before, during and after the procedures in select slice orientations. In this study, we have demonstrated that simultaneous measurements of 1-D myocardial motion and 1-D chamber blood flow for a given imaging slice can be obtained in a single breath-held acquisition using SPAMM n' EGGS. This represents a 50% speed-up in time compared with acquiring the motion and flow datasets separately. Parallel imaging methods could be used to further accelerate the acquisition speed by at least a factor of 2. While this will decrease the signal-to-noise ratio by a factor of $\sqrt{2}$, this loss in SNR can potentially be compensated by using a balanced steady-state free-precession–based pulse sequence in the future.

The SPAMM n' EGGS imaging protocol ensures perfect spatial and temporal registrations, and correlated measurements of the tagged myocardium and the chamber blood flow images. This feature may be useful to identify transient myocardial dysfunctions that lead to trans-valvular flow abnormalities in patients with IMR, LV hypertrophy, dilatative cardiomyopathy, LV reduction, and LV dyssynchrony, especially under stress. While it is true that the data are acquired over the course of multiple heart beats, physiologic transient events that occur during such stress studies will still be manifested in a correlated manner on both, the motion and the flow datasets because they are acquired simultaneously. If during these studies, the detection

of very rapid transient events takes precedence, the breath-hold time can be decreased at the cost of SNR or image resolution.

Phase contrast imaging pulse sequences could potentially provide information about blood velocity and myocardial displacement simultaneously. However, the velocity ranges that need to be accurately quantified for the myocardium (5–20 cm/s) and chamber blood (70–140 cm/s) are far apart. As a result, it is a challenge to find optimum V_{enc} that provides a dynamic range in image intensity with good sensitivity to both velocity ranges.

As seen in Figure 4, as the tagging flip angle increases from 45°–85° a proportionate improvement in the overall tag contrast and a simultaneous increase in the noise dominance in the flow signal is observed in the early part of the cardiac cycle. The 2-D Fourier transform of a typical SPAMM n' EGGS image has a central DC peak and two harmonic tagging peaks. The energy density of the tagging peaks is directly related to the tag contrast in the myocardium while the energy density of the DC peak is directly related to the strength of the reconstructed blood flow signal. For example, during 90°–90° SPAMM tagging, modulation of the complete longitudinal magnetization signal results in strong harmonic peaks and a negligibly small DC peak during the first few cardiac frames which in turn manifests into greater overall tag contrast and poor flow signal early in the cardiac cycle in the reconstructed tagged and flow images (see Fig. 3c). Conversely, during 45° −45° SPAMM, modulation of 50 % of the longitudinal magnetization results in relatively weaker harmonic peaks and a stronger DC peak during the first few cardiac frames which in turn manifests into relatively lower tag contrast and good flow signal early in the cardiac cycle in the reconstructed tagged and flow images (see Fig. 3a).

From Figure 4a, we find that the tag contrast obtained from the conventional scans are greater by nearly a factor of 1.5 to 3 early in the cardiac cycle as compared with the tag contrast in the images reconstructed from the SPAMM n' EGGS acquisitions. This is largely due to the fact that early in the cardiac cycle, higher imaging flip angles were used during the conventional scans as compared to the SPAMM n' EGGS acquisitions. However, qualitative inspection of the image quality in Figure 3b,c indicates good tag contrast and tag persistence in the SPAMM n' EGGS acquisitions with tagging flip angles of 65° and 90°.

From Figure 4b, we find that the noise dominance in the flow signal is much lower in the conventional scans than the SPAMM n' EGGS scans, especially early in the cardiac cycle. For a tagging flip angle of 45°, the noise estimate is approximately 2.5 times greater, while for a tagging flip angle of 85°, the noise estimate is nearly 24 times greater than conventional scans early in the cardiac cycle. We find from these curves, that for a tagging flip angle of 65°, the noise estimate after 100 ms is around 7 times greater and after 150 ms is around 5 times greater than conventional scans. From qualitative inspection of the flow images in Figure 3b, the image quality obtained with a tagging flip angle of 65° was sufficient for our application. If detailed examination of the flow signal earlier in the cardiac cycle is desired, the tagging flip angle can be decreased accordingly.

Experiments were performed on six normal volunteers to demonstrate the feasibility and accuracy of this technique. Measurements of myocardial strain and trans-valvular flow in small regions of interest were compared with measurements made using standard tagging and phase contrast imaging sequences separately (see Fig. 5; Table 1). These results demonstrate a close relation in the general trends of the curves obtained using both techniques. Slice misregistrations between acquisitions due to differential diaphragm positions during breath-holds may contribute to the differences in the measurements observed. In the future, to enable automatic strain computation in the myocardium, nonrigid registration-based tracking methods

(23), or phase-based tracking methods such as HARP (24,25) can be implemented on the magnitude images obtained from Eq. [2].

Combined tagged images with color flow (see Figs. 6, 7) provide good qualitative simultaneous visualizations of the two measurements. The quantitative time-evolution curves in Figure 8b demonstrates our ability to detect motion dysfunctions (decreased lateral longitudinal shortening in the region of infarction) and flow dysfunctions (regurgitant jet velocities), and to investigate their temporal correlations.

In conclusion, we have demonstrated a method that simultaneous acquisition of myocardial motion and chamber blood flow is possible within a single breath-hold using the SPAMM n' EGGS pulse sequence. The data obtained may be useful in the planning and evaluation of mitral-valve repair procedures.

ACKNOWLEDGMENTS

The authors thank Dr. Andrew J. Derbyshire for his insightful discussions and Ms. Kathy Lucas and Ms. Joni Taylor for their assistance with the animal studies.

REFERENCES

1. D'Andrea A, Caso P, Cuomo S, et al. Effect of dynamic myocardial dyssynchrony on mitral regurgitation during supine bicycle exercise stress echocardiography in patients with idiopathic dilated cardiomyopathy and 'narrow' QRS. Eur Heart J 2007;28:1004–1011. [PubMed: 17400608]
2. Borges MC, Colombo RC, Goncalves JG, Ferreira Jde O, Franchini KG. Longitudinal mitral annulus velocities are reduced in hypertensive subjects with or without left ventricle hypertrophy. Hypertension 2006;47:854–860. [PubMed: 16585417]
3. Araujo AQ, Arteaga E, Ianni BM, et al. Relationship between outflow obstruction and left ventricular functional impairment in hypertrophic cardiomyopathy: a Doppler echocardiographic study. Echocardiography 2006;23:734–740. [PubMed: 16999691]
4. Burgess MI, Fang ZY, Marwick TH. Role of diastolic dyssynchrony in the delayed relaxation pattern of left ventricular filling. J Am Coll Echocardiogr 2007;20:63–69.
5. Zerhouni EA, Parish DM, Rogers WJ, Yang A, Shapiro EP. Human heart: tagging with MR imaging —a method for noninvasive assessment of myocardial motion. Radiology 1988;169:59–63. [PubMed: 3420283]
6. Young AA, Imai H, Chang CN, Axel L. Two-dimensional left ventricular deformation during systole using magnetic resonance imaging with spatial modulation of magnetization. Circulation 1994;89:740–752. [PubMed: 8313563]
7. Pelc NJ, Drangova M, Pelc LR, et al. Tracking of cyclic motion with phase-contrast cine MR velocity data. J Magn Reson Imaging 1995;5:339–345. [PubMed: 7633112]
8. Wedeen VJ. Magnetic resonance imaging of myocardial kinematics. Technique to detect, localize, and quantify the strain rates of the active human myocardium. Magn Reson Med 1992;27:52–67. [PubMed: 1435210]
9. Jung B, Foll D, Bottler P, Petersen S, Hennig J, Markl M. Detailed analysis of myocardial motion in volunteers and patients using high-temporal-resolution MR tissue phase mapping. J Magn Reson Imaging 2006;24:1033–1039. [PubMed: 16947325]
10. van Dijk P. Direct cardiac NMR imaging of heart wall and blood flow velocity. J Comput Assist Tomogr 1984;8:429–436. [PubMed: 6725689]
11. Aletras AH, Balaban RS, Wen H. High-resolution strain analysis of the human heart with fast-DENSE. J Magn Reson 1999;140:41–57. [PubMed: 10479548]
12. Aletras AH, Ding S, Balaban RS, Wen H. DENSE: displacement encoding with stimulated echoes in cardiac functional MRI. J Magn Reson 1999;137:247–252. [PubMed: 10053155]
13. Kim D, Gilson WD, Kramer CM, Epstein FH. Myocardial tissue tracking with two-dimensional cine displacement-encoded MR imaging: development and initial evaluation. Radiology 2004;230:862–871. [PubMed: 14739307]

14. Kilner PJ, Yang GZ, Firmin DN. Morphodynamics of flow through sinuous curvatures of the heart. Biorheology 2002;39:409–417. [PubMed: 12122260]
15. Kilner PJ, Yang GZ, Wilkes AJ, Mohiaddin RH, Firmin DN, Yacoub MH. Asymmetric redirection of flow through the heart. Nature 2000;404:759–761. [PubMed: 10783888]
16. Wigstrom L, Ebbers T, Fyrenius A, et al. Particle trace visualization of intracardiac flow using time-resolved 3D phase contrast MRI. Magn Reson Med 1999;41:793–799. [PubMed: 10332856]
17. Chatzimavroudis GP, Oshinski JN, Pettigrew RI, Walker PG, Franch RH, Yoganathan AP. Quantification of mitral regurgitation with MR phase-velocity mapping using a control volume method. J Magn Reson Imaging 1998;8:577–582. [PubMed: 9626871]
18. Kozerke S, Schwitter J, Pedersen EM, Boesiger P. Aortic and mitral regurgitation: quantification using moving slice velocity mapping. J Magn Reson Imaging 2001;14:106–112. [PubMed: 11477667]
19. Axel L, Goncalves RC, Bloomgarden D. Regional heart wall motion: two-dimensional analysis and functional imaging with MR imaging. Radiology 1992;183:745–750. [PubMed: 1584931]
20. Amini, AA.; Prince, JL. Measurement of cardiac deformations from MRI: physical and mathematical models. Springer; New York: 2001. p. 344
21. McVeigh ER. MRI of myocardial function: motion tracking techniques. Magn Reson Imaging 1996;14:137–150. [PubMed: 8847969]
22. Fischer SE, McKinnon GC, Maier SE, Boesiger P. Improved myocardial tagging contrast. Magn Reson Med 1993;30:191–200. [PubMed: 8366800]
23. Ledesma-Carbayo MJ, Kybic J, Desco M, et al. Spatio-temporal nonrigid registration for ultrasound cardiac motion estimation. IEEE Trans Med Imaging 2005;24:1113–1126. [PubMed: 16156350]
24. Osman NF, Kerwin WS, McVeigh ER, Prince JL. Cardiac motion tracking using CINE harmonic phase (HARP) magnetic resonance imaging. Magn Reson Med 1999;42:1048–1060. [PubMed: 10571926]
25. Osman NF, Prince JL. Visualizing myocardial function using HARP MRI. Phys Med Biol 2000;45:1665–1682. [PubMed: 10870717]

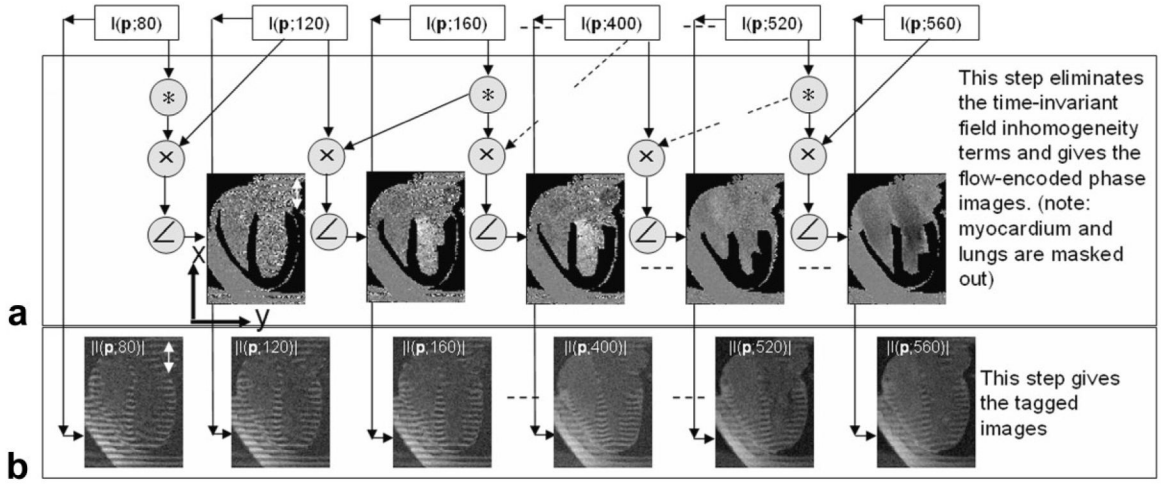

Figure 1.

Diagram representing the postprocessing steps used to reconstruct the tagged images and the chamber blood flow images from the reconstructed complex SPAMM n' EGGS images $I(\mathbf{p},t)$. **A:** A sliding-window phase-sensitive reconstruction (un-encoded images used as phase reference) used to isolate the blood flow velocity terms. **B:** The tagged images obtained from magnitude reconstruction.

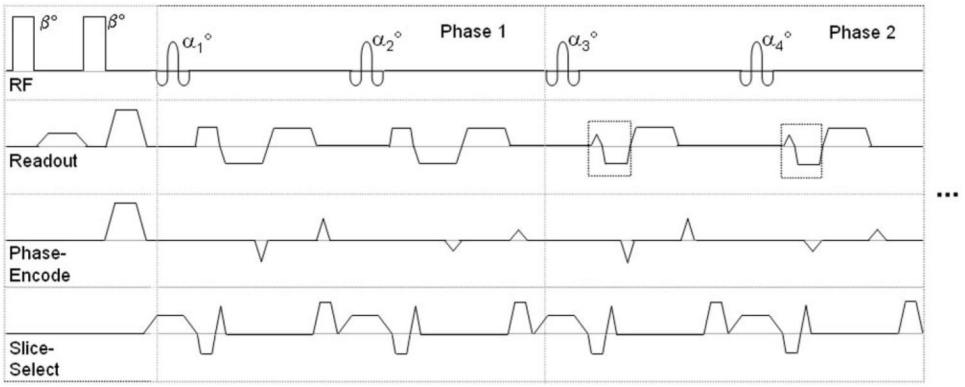

Figure 2.

Diagrammatic representation of a typical SPAMM n' EGGS pulse sequence. The views per cardiac phase were set to 2 for convenience of display. The actual value used typically varies from 3 to 5. Phase 1 represents the velocity unencoded reference acquisition, while phase 2 represents the velocity encoded acquisition. The rectangular boxes in phase 2 highlight the composite gradients obtained by adding the flow-encoding gradients to the existing flow compensating readout gradients.

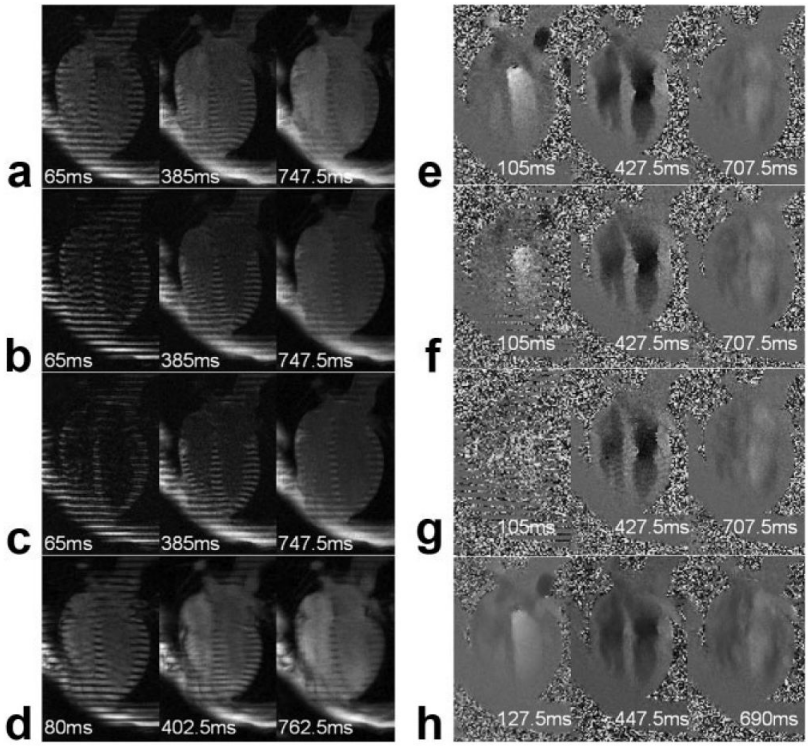

Figure 3.

a–d: Reconstructed tagged images at three representative time frames from SPAMM n' EGGS pulse sequence with tagging flip angle β of 45°, 65°, and 90° (a–c) and conventional tagging pulse sequence (d). **e–h:** Reconstructed flow images at three representative time frames from SPAMM n' EGGS pulse sequence with tagging flip angle β of 45°, 65°, and 90° (e–g) and conventional phase contrast pulse sequence (h).

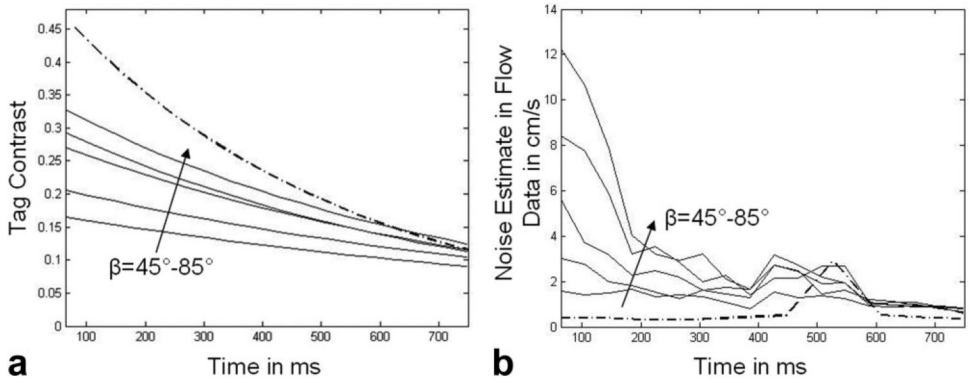

Figure 4.

a,b: Curves depicting tag contrast (a) and noise estimate (b) in the flow signal for SPAMM n' EGGS acquisitions with tagging flip angle β varying from 45° −90° (alternating solid and dotted lines), and conventional tagging and phase-contrast (dot-dashed) acquisitions.

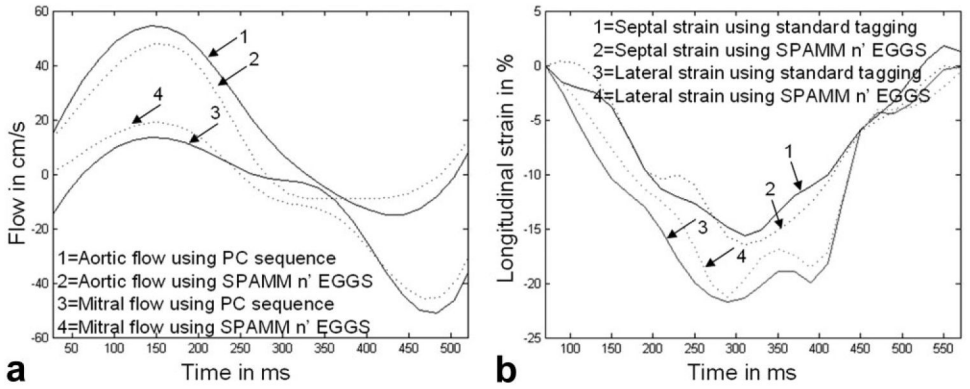

Figure 5.

a: Curves comparing the evolution of aortic and mitral flow averaged over a small region of interest obtained using SPAMM n' EGGS (see dotted line), and using standard phase contrast pulse sequence (see solid line). **b:** Curves comparing the evolution of longitudinal septal and lateral strain obtained using SPAMM n' EGGS (see dotted line), and using a standard tagging sequence (see solid line).

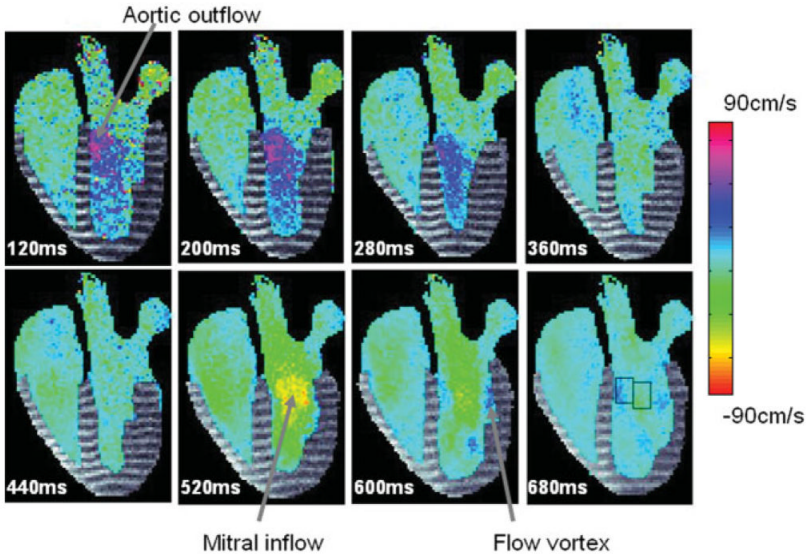

Figure 6.
A sequence of combined tag-flow images obtained in a normal volunteer from a single breath-held SPAMM n' EGGS acquisition. The colorbar depicts the hsv colormap used to scale the chamber blood flow data.

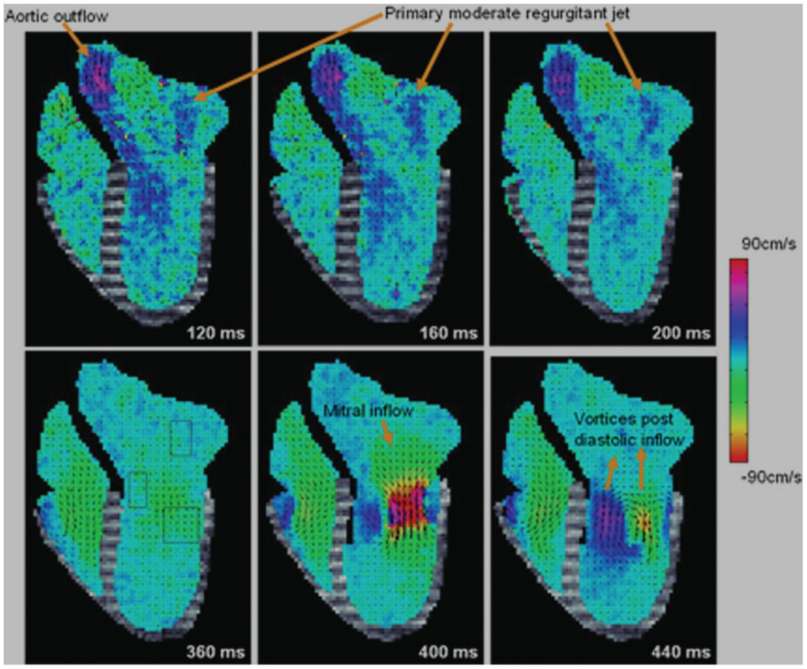

Figure 7.
Six representative time frames depicting combined motion–flow data obtained in two short breath-held acquisitions from a pig with moderate induced ischemic mitral regurgitation.

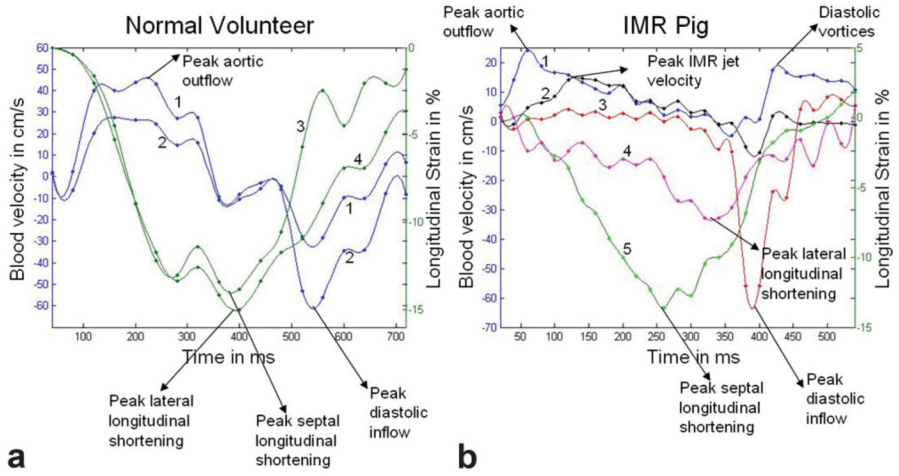

Figure 8.

a,b: Plots correlating the evolution of myocardial longitudinal strain (marked on the right axis) and longitudinal blood velocity (marked on the left axis) in a normal volunteer (a) and a pig with ischemic mitral regurgitation (b). In a, curves 1 and 2 correspond to the average aortic outflow and mitral inflow velocities respectively computed over rectangular regions of interest marked in Figures 6-8, while curves 3 and 4 correspond to the average septal and lateral longitudinal strains, respectively. In b, curves 1, 2, and 3 correspond to the average aortic outflow, ischemic mitral regurgitation (IMR) jet flow, and mitral inflow velocities respectively computed over rectangular regions of interest marked in Figures 7-4, while curves 4 and 5 correspond to the average lateral and septal longitudinal strains, respectively.

Table 1

Table Comparing Key Parameters of Interest Measured in Six Healthy Volunteers From Data Acquired Using SPAMM n' EGGS (SE) and Standard Tagging (ST) or Standard Phase Contrast (SPC) Sequences

	Peak septal longitudinal shortening (%)	Time to peak septal longitudinal shortening (ms)	Peak lateral longitudinal shortening (%)	Time to peak lateral longitudinal shortening (ms)	Peak aortic outflow (cm/s)	Time to peak aortic flow (ms)	Peak mitral inflow (cm/s)	Time to peak mitral inflow (ms)
	SE/ST	**SE/ST**	**SE/ST**	**SE/ST**	**SE/SPC**	**SE/SPC**	**SE/SPC**	**SE/SPC**
1	−16.5/−15.5	310/310	−21.2/−21.8	290/290	49/56	150/150	−45/−50	480/480
2	−14.3/−17	385/385	−15/−17.2	400/400	45/44	240/240	−65/−62	540/540
3	−14.8/−15.2	280/280	−17.5/−17.5	280/280	57/60	150/150	−55/−50	500/500
4	−19/−17.5	400/400	−20.5/−20.4	420/420	53/55	250/250	−62/−60	580/580
5	−15.3/−16.2	360/360	−18.6/−18.6	360/360	58/60	225/200	−60/−65	540/570
6	−15.8/−17	320/320	−20.3/−21.1	360/360	48/46	170/160	−52/−46	460/480